Chapter 3

The Optoelectronic Swept-Frequency Laser

3.1 Introduction

In this chapter we study the optoelectronic swept-frequency laser (SFL)—a feedback system that enables closed-loop control over the instantaneous optical frequency of a chirped semiconductor laser (SCL). Precisely linear frequency sweeps are of particular interest because of their applications in optical frequency-modulated continuous-wave (FMCW) reflectometry and 3-D imaging, as described in chapter 2. The SFL is a key component of an FMCW system since its characteristics directly affects important performance metrics. Specifically, the axial resolution and the maximum range are inversely proportional to the laser frequency tuning range and linewidth, respectively.

Mechanically tunable extended cavity lasers with large frequency excursions of about 10 THz have been used in medical tomographic applications to achieve range resolutions of about 10 μm [26, 48]. However, linewidths of tens of GHz, which are typical for such devices, limit ranging depths to just a few mm [49, 50]. Moreover, the mechanical nature of the frequency tuning limits the scan repetition rate and adds overall system complexity. Commercially available semiconductor laser (SCL) diodes, on the other hand, offer superior sub-MHz linewidths, corresponding to ranging depths of a few hundred meters, and can be frequency tuned with current [5], enabling precise chirp control with closed-loop feedback [1]. The small size and high

wall-plug efficiency of these devices makes them attractive for hand-held applications. The wide gain bandwidth of semiconductor quantum wells and the ability to fabricate SCLs with precisely controlled emission frequencies [4] make possible sophisticated imaging modalities such as multiple source FMCW [13, 14], described in chapter 4.

In this chapter we begin by analyzing the SCL-based optoelectronic SFL. We derive equations governing the SFL closed-loop operation, and describe a bias current predistortion algorithm that improves the SFL linearity. We discuss the SCLs that were used in our experiments and describe an amplitude control sub-system that suppresses the intensity modulation of a current-tuned SCL. We demonstrate closed-loop linear chirps at range of chirp rates and wavelengths, and show that the optoelectronic SFL is capable of generating arbitrary chirp profiles. We describe our collaborative efforts with Telaris Inc. to implement the feedback and predistortion functionality on an embedded electronic platform and commercialize the SFL. We conclude by demonstrating the use of the optoelectronic SFL in reflectometry and profilometry applications.

3.2 System Analysis

A schematic diagram of the optoelectronic SFL is shown in figure 3.1. The system comprises an SCL coupled to a Mach-Zehnder interferometer (MZI), a photodetector at the MZI output, a mixer that compares the phases of the photocurrent and the reference oscillator, and an integrator that processes the mixed-down signal and feeds it back into the SCL. The MZI measures the instantaneous chirp slope, and the feedback loop locks it to a constant value that is determined by the reference frequency, ensuring a perfectly linear chirp. An amplitude controller is used to keep the SCL intensity constant as its frequency is tuned with input current. We begin our analysis by noting an analogy between the SFL feedback and a phase-locked loop (PLL). We then derive its steady-state operating point and analyze small-signal deviations in the frequency domain. We introduce an iterative predistortion procedure that relaxes constraints on the optoelectronic feedback and enables locking at high chirp rates.

We conclude by discussing different SCL platforms and how they motivate the choice of an amplitude control element.

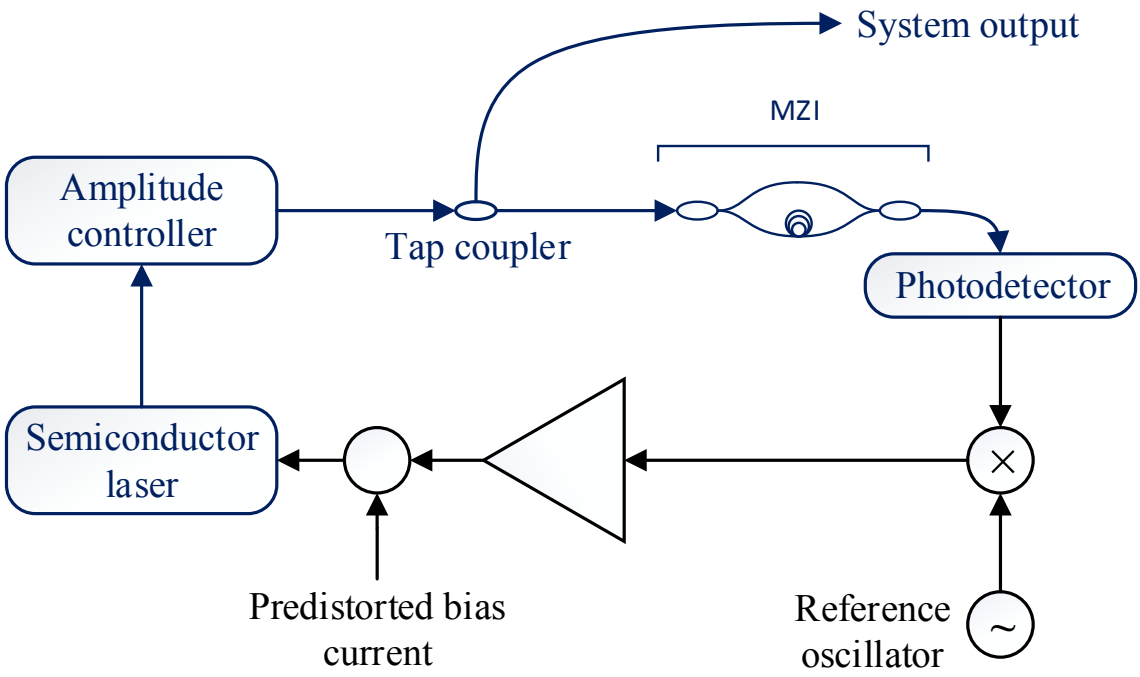

Figure 3.1: Schematic diagram of the SCL-based optoelectronic SFL

3.2.1 The Optoelectronic SFL as a PLL

We first demonstrate that the optoelectronic SFL acts like a phase-locked loop in the small-signal approximation. We begin by assuming that the SCL bias current predistortion is perfect, so that the output chirp is precisely linear. We will later remove this assumption by treating post-predistortion residual nonlinearity as additional phase noise. The electric field of a linear chirp is given by equation (2.1), replicated below without the rect function that models the chirp's finite duration:

$$e(t) = \cos\left[\phi_{SFL}(t)\right], \text{ and } \phi_{SFL}(t) \equiv \phi_0 + \omega_0 t + \frac{\xi t^2}{2}, \tag{3.1}$$

where $\phi_{SFL}(t)$ is an overall electric field phase that is quadratic in time, ξ is the slope of the optical chirp, and ϕ_0 and ω_0 are the initial phase and frequency, respectively.

The instantaneous optical frequency is therefore the derivative of $\phi_{SFL}(t)$:

$$\omega_{SFL}(t) = \frac{d\phi_{SFL}(t)}{dt}. \tag{3.2}$$

A tap coupler is used to launch a small amount of the chirped light into a MZI with delay τ. The beat signal between $e(t)$ and $e(t-\tau)$ is measured by a photodetector, so that its output current is given by:

$$\begin{aligned} i_{\mathrm{PD}} &\propto \cos\left[\phi_{SFL}(t) - \phi_{SFL}(t-\tau)\right] \\ &\approx \cos\left(\tau\frac{d\phi_{SFL}}{dt}\right) = \cos\left[\phi_{PD}(t)\right], \text{ and } \phi_{PD}(t) \equiv \omega_{SFL}(t)\tau, \end{aligned} \tag{3.3}$$

and we have ignored DC terms for simplicity. Equation (3.3) shows that if the MZI delay is chosen small enough, the photocurrent phase ϕ_{PD} is proportional to the instantaneous SCL frequency. Consider a small-signal $\delta s(t)$ at the input to the integrator in figure 3.1. Assuming that the integrated signal is small enough so that the SCL tuning remains linear, the associated change in the photocurrent phase $\delta\phi_{PD}(t)$ is given by:

$$\delta\phi_{PD}(t) = \delta\omega_{SFL}(t)\tau \propto \int^{t} \delta s(u)\, du, \tag{3.4}$$

where $\delta\omega_{SFL}(t)$ is the SCL frequency shift due to the additional bias current. The photocurrent phase shift is proportional an integral of $\delta s(t)$ in the small-signal approximation, which is the defining characteristic of an ideal voltage-controlled oscillator (VCO). The integrator, the SCL, the MZI, and the photodetector may therefore be lumped together and treated as a VCO. These elements are highlighted in figure 3.2.

The action of the optoelectronic SFL is therefore to lock the phase of the effective VCO to a reference electronic oscillator.

$$\phi^{L}_{PD}(t) = \phi_{REF}(t) + 2\pi n \implies \omega^{L}_{SFL}(t)\tau = \omega_{REF}t + \phi_{REF}(0) + 2\pi n,\ n \in \mathbb{Z}, \tag{3.5}$$

where $\phi_{REF}(t)$ is the overall phase of the reference oscillator and ω_{REF} is its fre-

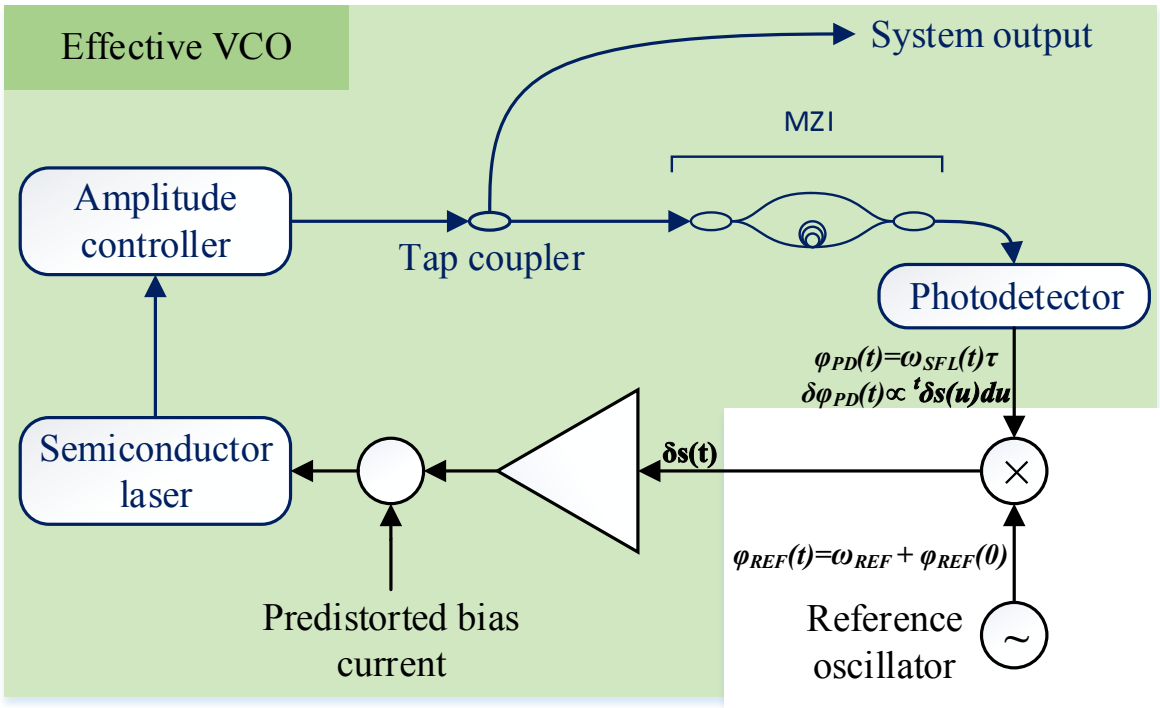

Figure 3.2: Elements of the optoelectronic SFL lumped together as an effective VCO

quency. We use the superscript L to denote quantities associated with the locked state. The feedback maintains a precisely linear chirp with a chirp rate and initial optical frequency given by

$$\xi^L = \frac{\omega_{REF}}{\tau} \text{ and } \omega_0^L = \frac{\phi_{REF}}{\tau} + n\frac{2\pi}{\tau}. \tag{3.6}$$

We recognize that $\frac{2\pi}{\tau}$ is just the free spectral range (FSR) of the MZI. Equation (3.5) describes a family of closed-loop linear chirp solutions indexed by the integer n. The solutions are separated in optical frequency by the MZI FSR, and the choice of a particular one depends on the free-running chirp parameters. Specifically, the system will lock to the solution whose initial optical frequency most closely matches the free-running optical frequency.

At the end of the scan the system is taken out of lock, and the SCL current is brought back to its original value. The chirp is consequently re-started and lock re-established. As a result, if the fluctuations in the free-running initial optical frequency are great enough, for example, due to imperfect SCL temperature control,

the SFL will lock to a different system solution during subsequent scans. To obtain repeatable chirps, it is therefore necessary to choose the MZI FSR large enough, so that fluctuations in the free-running chirp are localized around a single closed-loop solution.

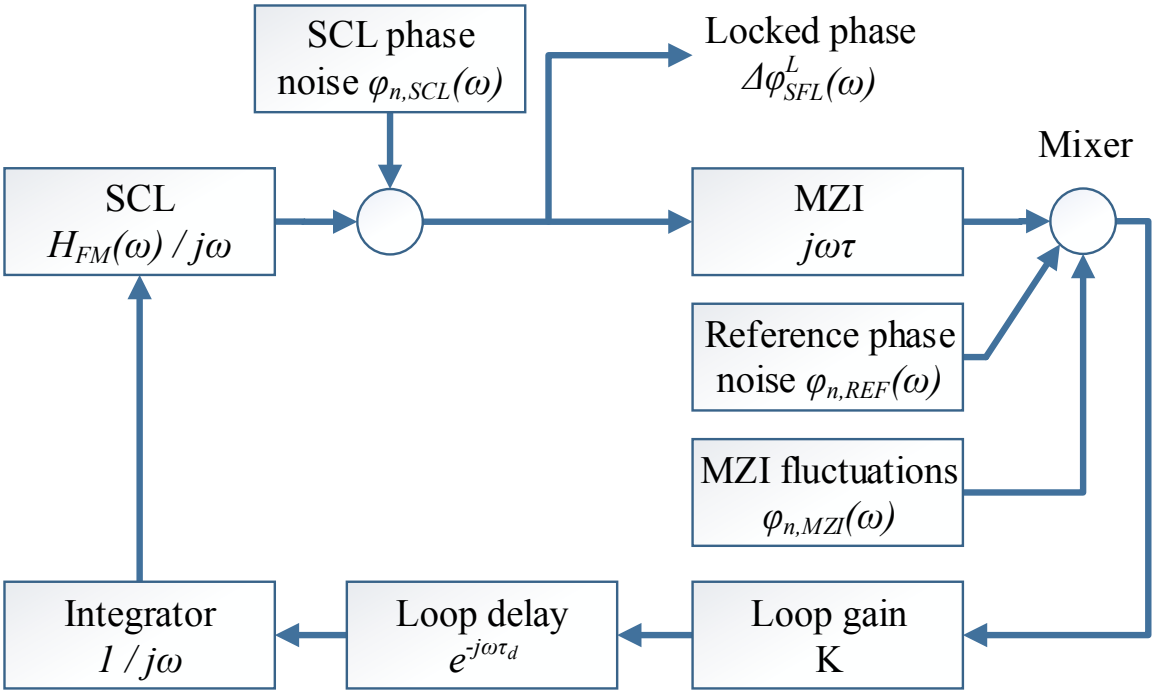

Figure 3.3: Small-signal frequency-domain model of the optoelectronic SFL

3.2.2 Small-Signal Analysis

The preceding discussion establishes an analogy between the optoelectronic SFL and a phase-locked loop. We now apply small-signal analysis [1, 51] to study fluctuations about the locked state in the Fourier domain, with the Fourier frequency denoted by ω. The small-signal model of the feedback loop is shown in figure 3.3. The loop variable is the deviation of the optical phase from its steady-state value,

$$\phi^{L}_{SFL}(t) = \phi_0 + \frac{\phi_{REF}}{\tau}t + n\frac{2\pi}{\tau}t + \frac{\omega_{REF}t^2}{2\tau}. \tag{3.7}$$

The transfer function of the SCL is $\frac{H_{FM}(\omega)}{j\omega}$, where $H_{FM}(\omega)$ is the frequency modulation (FM) response of the SCL, normalized to unity at DC, and $\frac{1}{j\omega}$ results from the

integral relationship between the SCL bias current and the optical phase. The FM response of single-section SCLs is characterized by a competition between thermal and electronic tuning mechanisms [52–55]. At low modulation frequencies, the optical frequency decreases with rising bias current due to increased junction heating. At higher modulation frequencies, carrier tuning dominates, and the optical frequency is increased with rising bias current. As a result, the FM response of the SCL undergoes a phase reversal in the Fourier frequency range of $0.1 - 10$ MHz. This phenomenon is the dominant bandwidth limitation in the optoelectronic SFL [7, 9].

For frequencies much smaller than its free spectral range, the MZI can be approximated as an ideal optical phase differentiator with gain τ (this is the same approximation as in equation (3.3)) [56]. The total DC loop gain K is given by the product of the gains of all the loop elements—laser, photodetector, mixer, integrator, and other electronic circuits that are not explicitly shown. The loop propagation delay τ_d is on the order of tens of ns. While it does add to the loop phase response at higher frequencies, around the feedback bandwidth its contribution is small compared to the phase acquired due to the SCL FM response.

The optical phase noise of the SCL and the optical phase excursion due to residual nonlinearity are lumped together and denoted by $\phi_{n,SCL}(\omega)$. The phase noise of the reference oscillator and the phase noise introduced by environmental fluctuations in the MZI are denoted by $\phi_{n,REF}(\omega)$ and $\phi_{n,MZI}(\omega)$, respectively. Going around the loop, we write a frequency-domain expression for the locked phase deviation $\Delta\phi^L_{SFL}(\omega)$ from the steady state.

$$\begin{aligned}\Delta\phi^L_{SFL}(\omega) = \phi_{n,SCL}(\omega) - K\frac{H_{FM}(\omega)e^{-j\omega\tau_d}}{\omega^2}\left[\phi_{n,REF}(\omega) + \phi_{n,MZI}(\omega)\right] \\ + K\tau\frac{H_{FM}(\omega)e^{-j\omega\tau_d}}{j\omega}\Delta\phi^L_{SFL}(\omega)\end{aligned} \tag{3.8}$$

Solving for $\Delta\phi^L_{SFL}(\omega)$ yields

$$\begin{aligned}\Delta\phi^L_{SFL}(\omega) = &\frac{j\omega}{j\omega + K\tau H_{FM}(\omega)e^{-j\omega\tau_d}}\phi_{n,SCL}(\omega) \\ &+ \frac{1}{j\omega\tau} \times \frac{K\tau H_{FM}(\omega)e^{-j\omega\tau_d}}{j\omega + K\tau H_{FM}(\omega)e^{-j\omega\tau_d}} \left[\phi_{n,REF}(\omega) + \phi_{n,MZI}(\omega)\right].\end{aligned} \tag{3.9}$$

We observe that for frequencies within the loop bandwidth, the residual phase deviation tracks the reference oscillator and MZI noise, suppressed by the term $j\omega\tau$,

$$\Delta\phi^L_{SFL}(\omega \ll K\tau) \approx \frac{\phi_{n,REF}(\omega) + \phi_{n,MZI}(\omega)}{j\omega\tau}. \tag{3.10}$$

For frequencies outside the loop bandwidth, the residual phase deviation is given by the free-running phase noise term,

$$\Delta\phi^L_{SFL}(\omega \gg K\tau) \approx \phi_{n,SCL}(\omega). \tag{3.11}$$

From equation (3.10) it is clear that there are three considerations involved in the generation of precisely linear chirps: (1) using an electronic oscillator with low phase noise, (2) stabilizing the MZI against acoustic and thermal fluctuations, and (3) picking a large τ.

High quality electronic oscillator integrated circuits are widely available. In our systems we use direct digital synthesis (DDS) oscillators because they offer excellent phase and frequency stability, precise control of the reference frequency, and broad frequency tuning. The latter is useful in generating a wide range of chirp rates.

Active and passive interferometer stabilization techniques are well known, and include locking the delay to a reference laser using a fiber stretcher [57], athermal design of the MZI waveguides [58], and the use of vibration-damping polymers in interferometer packaging [59], to name a few. In our systems we use fiber-based MZIs packaged with sheets of Sorbothane®.

The choice of MZI delay is constrained by the free-running frequency fluctuations of the SCL, as discussed in section 3.2.1. In our systems we choose the largest

τ that yields repeatable chirps from scan to scan. For distributed-feedback laser (DFB) systems we use a delay from 5ns to as much as 30 ns, depending on the laser quality. Systems based on vertical-cavity surface-emitting lasers (VCSELs) possess more frequency jitter, and we therefore use MZIs with delays of about 1 ns.

3.2.3 Bias Current Predistortion

So far we have assumed that the SCL bias current is predistorted so that the chirp is sufficiently linear for lock acquisition. In this section we describe a predistortion procedure based on a simple nonlinear tuning model [1]. Even though the model is inaccurate, and a single use of this procedure does not yield a linear chirp, it is possible to achieve the desired linearity through iteration.

We model the nonlinear current-frequency relation of an SCL by introducing a tuning constant K that is a function of the SCL modulation current.

$$\omega_{SFL}(t) = \omega_0 + i(t)K[i(t)], \tag{3.12}$$

where ω_0 is the initial SCL frequency due to some bias current, and $i(t)$ is the deviation from that bias. To characterize the chirp we calculate the spectrogram of the MZI photocurrent. The spectrogram allows us to extract the instantaneous photocurrent frequency, found by differentiating the photocurrent phase in equation (3.3)

$$\omega_{PD}(t) = \frac{d\phi_{PD}(t)}{dt} = \tau\frac{d\omega_{SFL}(t)}{dt}. \tag{3.13}$$

Plugging in equation (3.12), we arrive at

$$\omega_{\mathrm{PD}}(t) = \tau\frac{d\omega_{SFL}(t)}{dt} = \tau\left[K(i) + iK'(i)\right]\frac{di(t)}{dt} = S(i)\frac{di(t)}{dt}, \tag{3.14}$$

where $S(i) \equiv K(i) + iK'(i)$. The function $S(i)$ describes the nonlinear tuning of the SCL and can be measured by launching a linear current ramp into the SCL and using

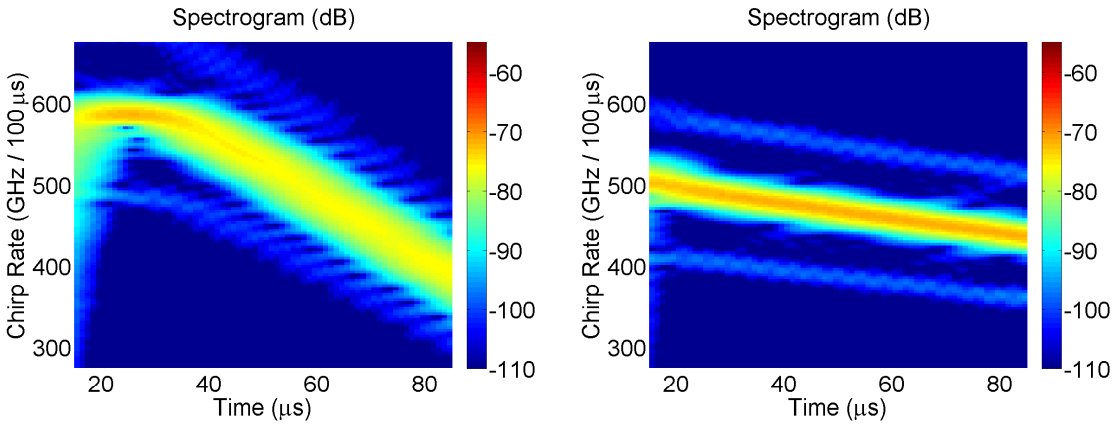

(a) Current ramp chirp spectrogram (b) Predistorted chirp spectrogram

Figure 3.4: Single predistortion results

a spectrogram to calculate $\omega_{\mathrm{PD}}(t)$. Then,

$$S(i) = \frac{\omega_{\mathrm{PD}}\left[t(i)\right]}{\alpha}, \tag{3.15}$$

where α is the current ramp slope. We use equation (3.14) to write a differential equation for the SCL modulation current

$$\frac{di(t)}{dt} = \frac{\tau}{S(i)} \frac{d\omega_{SFL,d}}{dt}, \tag{3.16}$$

where $\omega_{SFL,d}(t)$ is the desired optical chirp. We solve this equation numerically to find the current that will generate the desired tuning behavior $\omega_{SFL,d}(t)$.

The outlined procedure was used to predistort the current for a 1.55 μm VCSEL chirping 475 GHz in 100 μs. According to equation (3.13), a perfectly linear chirp is described by a flat photocurrent spectrogram. Figure 3.4a shows the spectrogram corresponding to a current ramp that was used to characterize $S(i)$. The y-axis has been rescaled by τ to show the instantaneous chirp rate. Figure 3.4b shows the spectrogram corresponding to the predistorted waveform, confirming the improvement in linearity.

Figure 3.4b is not perfectly flat, meaning that the corresponding optical chirp is not perfectly linear. The reason is that the tuning model is incomplete—it fails to cap-

ture dynamic tuning behavior, e.g., the competition between thermal and electronic tuning mechanisms described in section 3.2.2. Even though the model is incomplete, its application yields an improvement in chirp linearity. It stands to reason that iterative application of the model may yield additional improvements in chirp linearity. Iterative application means that we use the previous current predistortion to re-characterize the function $S(i)$, and calculate the next approximation by again solving equation (3.16). This process is repeated until the ensuing optical chirp is perfectly linear. We can combine equation (3.16) and equation (3.14) to write down the differential equation that can be used to calculate the n^{th}-order predistortion $i_n(t)$ from the preceding order predistortion, $i_{n-1}(t)$, and the corresponding photocurrent frequency measurement $\omega_{PD,n-1}(t)$.

$$\frac{di_n(t)}{dt} = \frac{\xi_d \tau}{\omega_{PD,n-1}\left[t_{n-1}(i_n)\right]} \times \frac{di_{n-1}}{dt}, \tag{3.17}$$

where ξ_d is the desired chirp rate, and $t_{n-1}(i)$ is the inverse of the i_{n-1}-th predistortion.

We have found that using a fourth-order predistortion is sufficient. The results are shown in figure 3.5. Each successive predistortion results in a chirp that is closer to the desired tuning characteristic, so that by the fourth order we arrive at a sufficiently linear chirp.

It is possible to further simplify the predistortion procedure. In equation (3.17) we evaluate the photocurrent frequency at time $t_{n-1}(i_n) = i_{n-1}^{-1}(i_n)$. It stands to reason that once the difference between successive predistortions is small enough, the photocurrent frequency may be evaluated just at time t,

$$\frac{di_n(t)}{dt} = \frac{\xi_d \tau}{\omega_{PD,n-1}(t)} \times \frac{di_{n-1}}{dt}. \tag{3.18}$$

This procedure makes sense intuitively—the slope of the previous predistortion is scaled by the ratio of the desired photocurrent frequency to the instantaneous photocurrent frequency. If the chirp is too fast, then the ratio will be less than one, slowing down the sweep at that particular time. Likewise, if the chirp is too slow, the

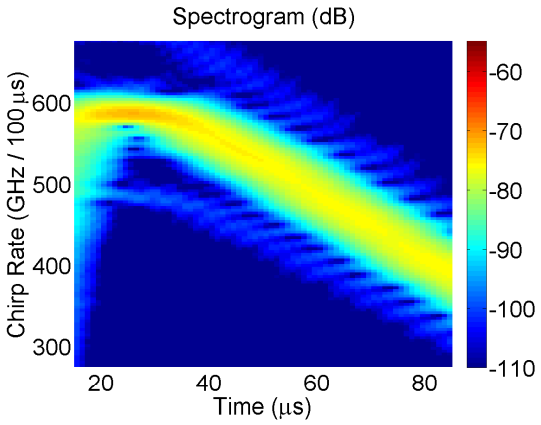

(a) Zeroth-order predistortion (current ramp) spectrogram

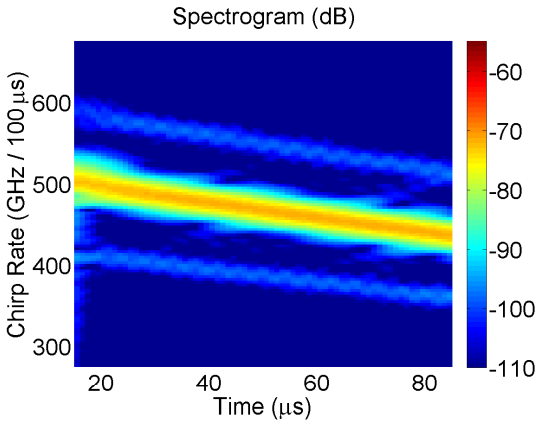

(b) First-order predistortion spectrogram

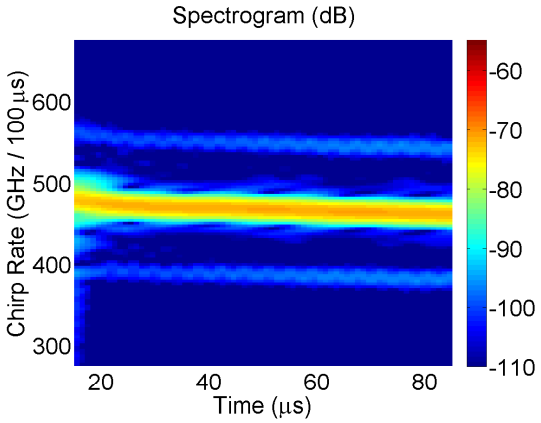

(c) Second-order predistortion spectrogram

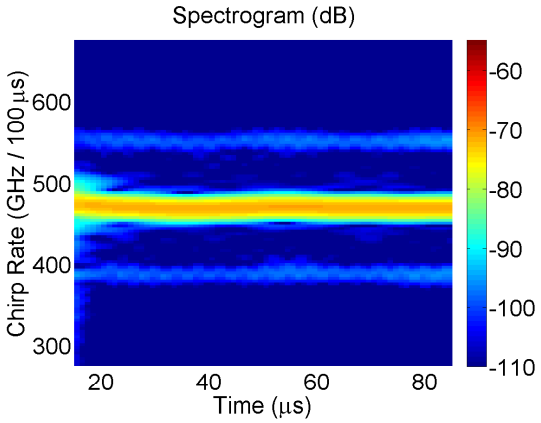

(d) Third-order predistortion spectrogram

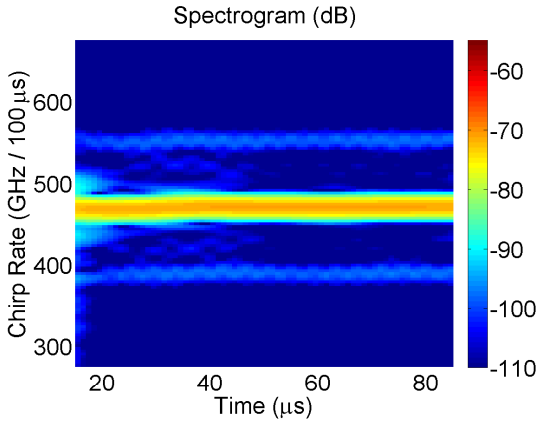

(e) Fourth-order predistortion spectrogram

Figure 3.5: Iterative predistortion results

ratio will be greater than unity, speeding it up.

This procedure is simpler computationally—it does not involve inverses, and therefore avoids interpolation. The differential equation (3.18) itself is simpler as well, since the right hand side no longer depends on i_n. We motivated these simplifications with the assumption that the successive predistortions are already close to each other. It is the case, however, that the simplified procedure works well in practice, and demonstrates the same rate of convergence as the original scheme, even if iterated starting at the linear current ramp. As part of our collaboration with Telaris Inc. to commercialize the optoelectronic SFL, we have implemented the simplified predistortion procedure on a microcontroller. The full predistortion procedure would have been significantly more difficult to realize in the computationally-limited embedded environment.

3.3 Design of the Optoelectronic SFL

3.3.1 SCL Choice

The choice of the semiconductor laser to use in the optoelectronic SFL is dependent upon the desired chirp bandwidth and linewidth. Distributed-feedback lasers (DFB) are inherently single-mode, possess a stable polarization, and a narrow linewidth of hundreds of kHz to a $\sim$ 1 MHz. The chirp ranges of commercially-available DFB lasers depend on the emission wavelength. In our experience, 1550 nm DFB lasers are limited in chirp range to about 100 GHz. The frequency chirp range increases with decreasing wavelength, and we have found that DFB lasers in the 1060 nm range can be current-tuned over a spectral range of about 200 GHz. The output power of DFB lasers is usually in the tens of mW.

When compared to DFBs, vertical-cavity surface-emitting lasers (VCSELs) are much cheaper, and generally tune over greater regions of the optical spectrum. We have tested VCSELs at wavelengths of 1550 nm, 1310 nm, 1060 nm, and 850 nm. We measured chirp bandwidths of $\sim$ 500 GHz at 1550 nm, $\sim$ 1 THz at 1310 nm,

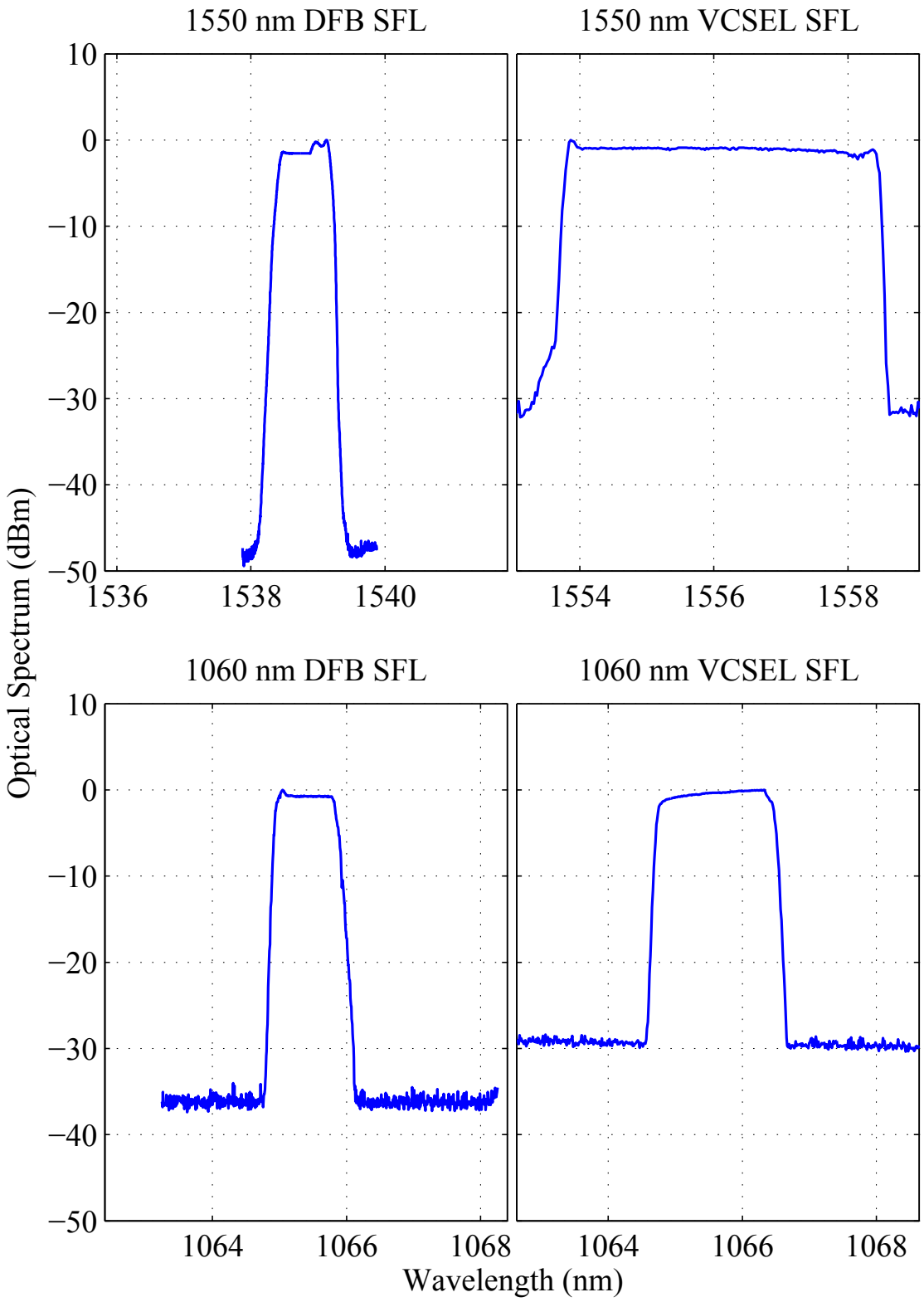

Figure 3.6: Measured optical spectra of DFB and VCSEL SFLs at wavelengths of 1550 nm and 1060 nm

$\sim$ 400 GHz at 1060 nm, and $\sim$ 1.5 THz at 850 nm. The 1060 nm VCSEL breaks the pattern, possibly because this is the least-developed VCSEL wavelength. Because of their short cavity lengths, VCSELs have broader linewidths of a few tens of MHz, and suffer from a reduced frequency stability. The reduced stability necessitates the use of shorter MZIs in the SFL feedback, increasing the closed-loop residual phase error, as described in section 3.2.2. In addition, VCSELs possess significantly lower powers of hundreds of μW to a few mW. As a result, VCSEL-based SFLs require amplitude control elements capable of providing optical gain, as described in section 3.3.2. Due to the circular symmetry of the VCSEL cavity, these devices sometimes have polarization instability and polarization mode hops [60], limiting their use in applications requiring polarization control. Nevertheless, VCSELs remain extremely attractive as swept sources in imaging and ranging applications due to their broad chirp bandwidths.

The optical spectra of the locked optoelectronic SFLs based on some of the SCLs discussed above are shown in figure 3.6. Swept sources based on 1310 nm and 850 nm VCSELs are currently being developed.

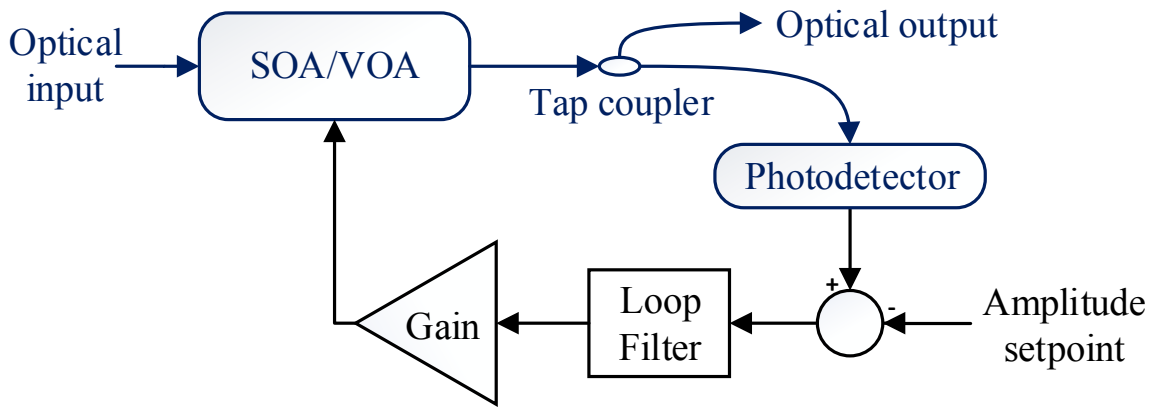

Figure 3.7: Schematic diagram of the amplitude controller feedback system

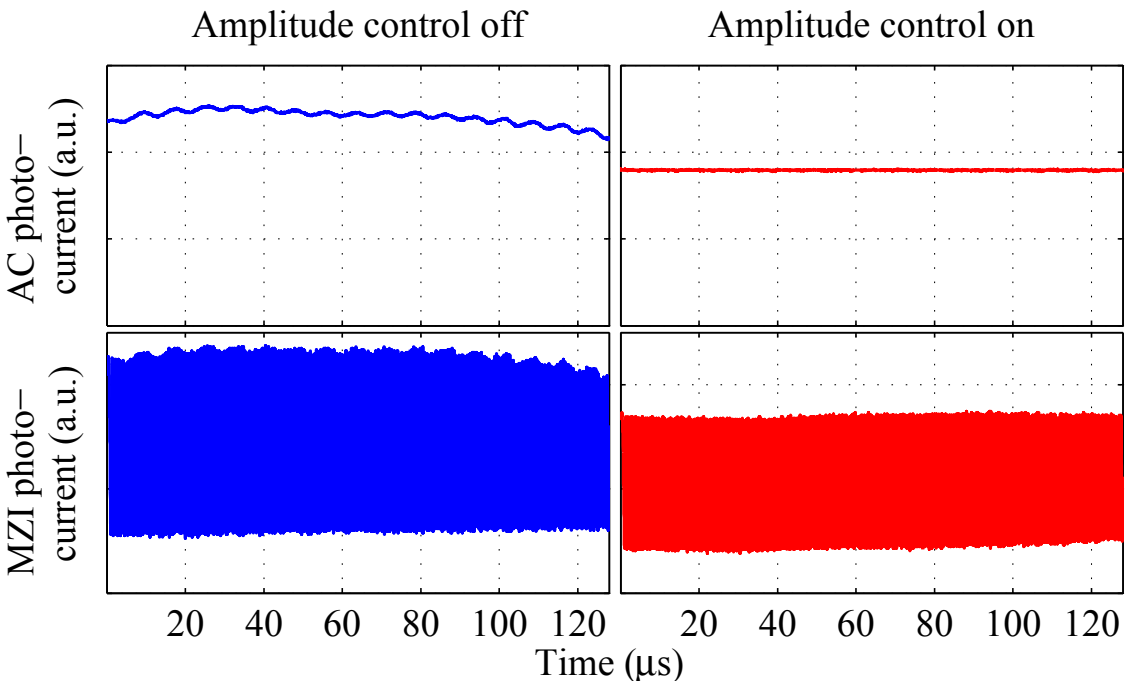

Figure 3.8: Comparison between the off(blue) and on(red) states of the SOA amplitude controller

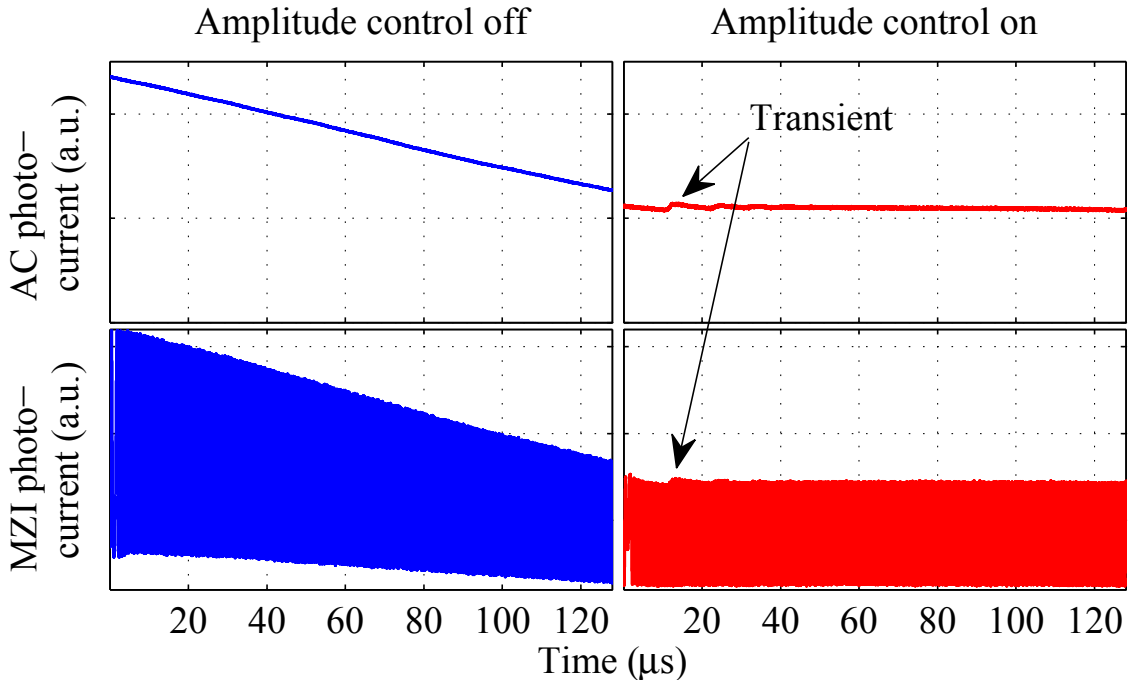

Figure 3.9: Comparison between the off(blue) and on(red) states of the VOA amplitude controller

3.3.2 Amplitude Control

As the SCL current is swept to produce a frequency chirp, the light undergoes undesired amplitude modulation. To overcome this effect, we place an amplitude controller after the SCL. The amplitude controller is a feedback system, shown in figure 3.7, that uses an intensity modulator and a tap photodetector to measure the instantaneous optical intensity, and lock it to a constant value. In our systems we have used two different intensity modulation elements—semiconductor optical amplifiers (SOAs) and variable optical attenuators (VOAs) based on electro-optical ceramics [61]. The SOAs provide optical gain, have GHz-range modulation bandwidths [62], but require temperature control and heat sinking. Furthermore, additional optical isolation is necessary to prevent lasing. VOAs solutions are cheaper and more compact because they do not generate excess heat, but they are also much slower, with sub-MHz modulation bandwidths. Because VOAs are passive devices, they are only practical for use with SCLs that emit sufficiently high optical powers. We use SOAs with VCSEL-based systems, which serves the dual purpose of amplitude control and optical amplification of the weak VCSEL output, and reserve the use VOAs for DFB-based SFLs.

The effect of the SOA-based amplitude controller on a chirped VCSEL input is shown in figure 3.8. The amplitude controller feedback signal is shown in the top panels and the MZI photocurrent is plotted in the bottom panels. When the amplitude controller is turned on, the intensity of the input into the MZI becomes fixed, suppressing the fluctuations in the MZI signal envelope. Corresponding plots for the DFB-VOA combination are shown in figure 3.9. Because the VOA is considerably slower than the SOA, transient effects appear in the beginning of the scan.

3.3.3 Electronics and Commercialization

As part of our collaboration with Telaris Inc., the company has commercialized the optoelectronic SFL. The chirped diode laser (CHDL) system offered by Telaris Inc. is a stand-alone SFL that is controlled by a computer through a USB port. The feedback electronics are implemented on a pair of printed circuit boards (PCBs),

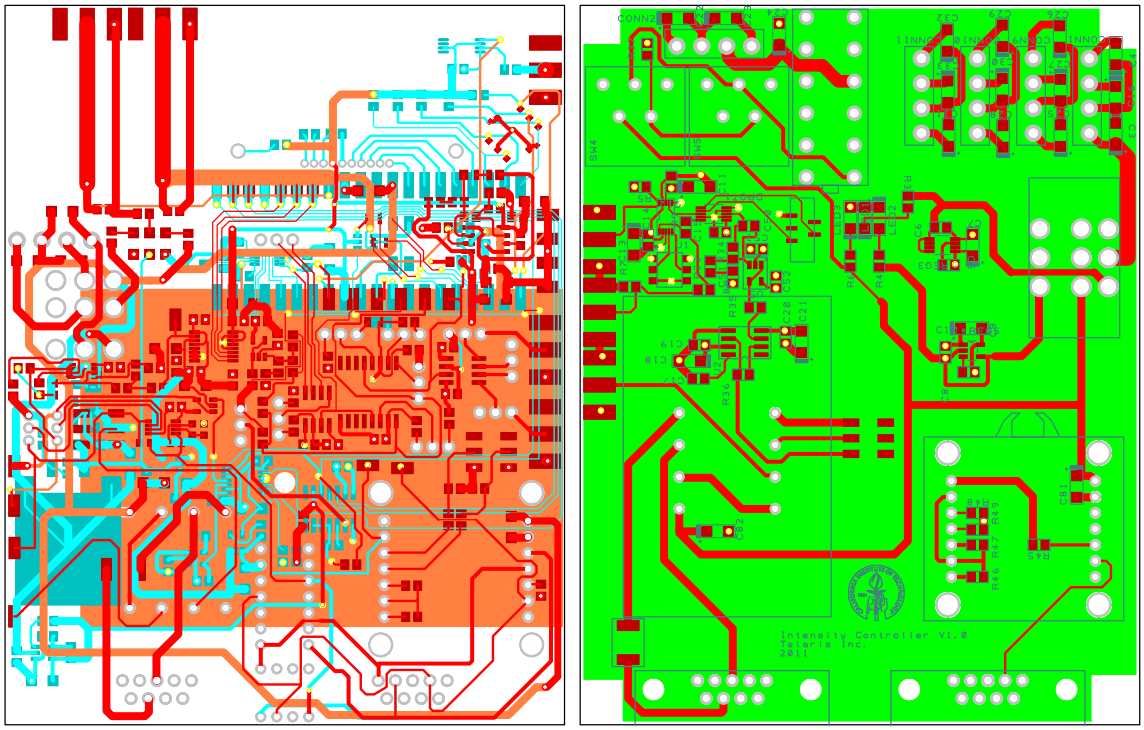

(a) SFL feedback PCB (b) Amplitude controller PCB

Figure 3.10: Optoelectronic SFL printed circuit board layouts

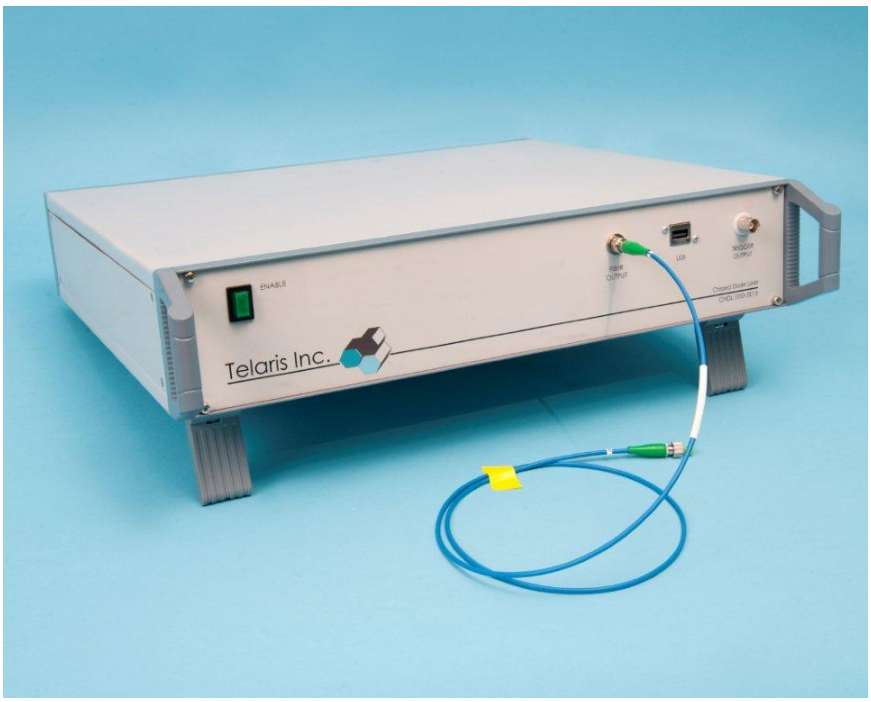

Figure 3.11: The 1550 nm CHDL system.

shown in figure 3.10. The boards include low-noise current sources and temperature controllers for the SCL and the SOA-based amplitude controller, a direct digital synthesis (DDS) chip to provide a frequency-agile reference oscillator, a 1 μs sampling rate digital-to-analog converter to generate predistortion waveforms, an offset-trimmed multiplier, and digital potentiometers to provide control over the various feedback gain and filter parameters. Calculating spectrograms for the predistortion procedure is a computationally-intensive task. Instead, the MZI signal is digitized using a comparator, and its instantaneous frequency is calculated by counting the number of zero-crossings that occur in a specified time window. This hardware-assisted predistortion measurement, along with the simplified algorithm described in section 3.2.3, enables rapid predistortion of the SCL bias current in an embedded environment. The entire system is controlled by an 8-core microcontroller. Parallel cores provide deterministic timing that is necessary for the simultaneous processing of the MZI signal and generation of the predistortion waveform. The system uses an acoustically-isolated fiber MZI to generate the feedback signal. The VCSEL-based 1550 nm CHDL system is shown in figure 3.11, and is capable of generating precisely linear chirps exceeding 500 GHz in bandwidth, at a maximum rate of 10 kHz.

3.4 Experimental Results

3.4.1 Precisely Controlled Linear Chirps

The optoelectronic SFL is turned on by first iterating the predistortion procedure, as described in section 3.2.3, with the MZI feedback gain set to zero. The MZI photocurrent spectra at different steps of this process are shown in figure 3.12. The x-axis has been scaled by the MZI FSR to correspond to the chirp rate ξ. Successive predistortion steps lead to a narrowing of the signal peak at the desired chirp rate. By the 3^{rd} predistortion, the signal peak width has achieved the transform limit $\frac{1}{\tau T}$, and additional predistortion steps reduce the noise pedestal. Once sufficient linearity is achieved with the predistortion, the feedback gain is turned on, and the SFL acquires

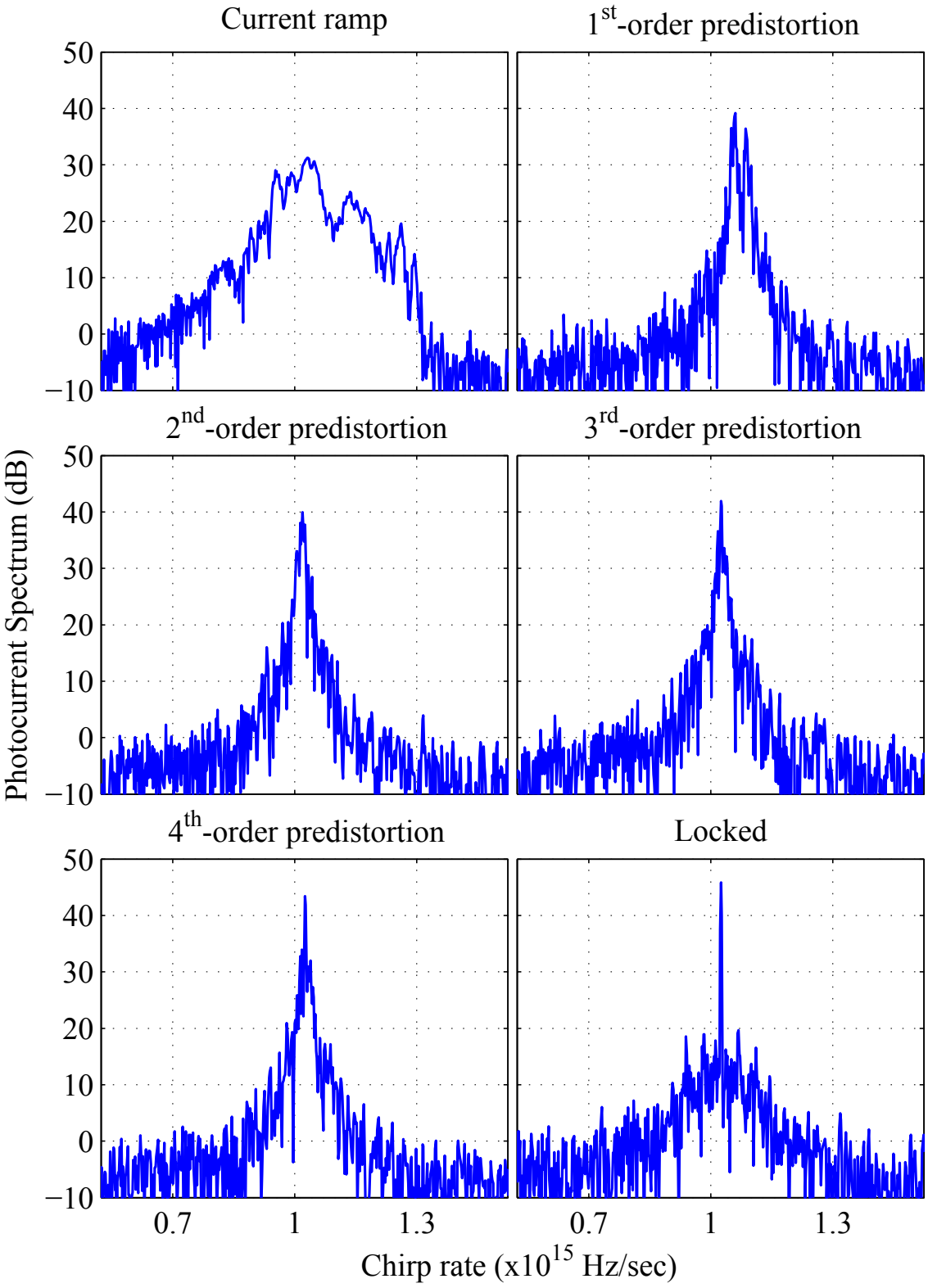

Figure 3.12: MZI photocurrent spectrum during the predistortion process and in the locked state

lock, yielding a constant chirp slope and a fixed starting frequency. The locked spectrum is characterized by a transform-limited peak with a low noise pedestal.

The chirp rate of the optoelectronic SFL is controlled by tuning the frequency of the electronic reference oscillator. The systems that we have built are capable of generating linear chirps with rates that are tunable over a decade. The locked spectra at different chirp rates of an optoelectronic SFL based on a 1550 nm DFB laser are shown in figure 3.13a. Corresponding spectra for a 1550 nm VCSEL system are shown in figure 3.13b, for a 1060 nm DFB system in figure 3.13c, and for a 1060 nm VCSEL system in figure 3.13d. The x-axis in all the plots corresponds to the chirp rate.

3.4.2 Arbitrary Chirps

So far we have focused on precisely linear chirps. The optoelectronic feedback technique can be extended in a straightforward way to generate arbitrary frequency chirps [1]. The predistortion procedure is modified to include time-dependence in the desired chirp rate ξ_d in equation (3.17) and equation (3.18). The integral of $\xi_d(t)$ gives the desired optical frequency vs. time function. Similarly, the locking frequency ω_{REF} becomes a function of time. The locked optical frequency evolution of the SFL will therefore be given by

$$\omega_{SCL}(t) = \frac{1}{\tau}\int_0^t \omega_{REF}(t)dt + \frac{\phi_{REF}}{\tau} + n\frac{2\pi}{\tau}, \tag{3.19}$$

where ϕ_{REF} is again the DC phase of the reference oscillator, and the integer n indexes the family of possible locked behaviors.

We have demonstrated this principle experimentally by generating quadratic and exponential optical frequency chirps using a DFB-based SFL at 1550 nm. For the quadratic chirp, we varied the reference frequency between 1.43 and 4.29 MHz, corresponding to a linear variation of the chirp rate from 50 to 150 GHz/ms. The measured photocurrent spectrogram in figure 3.14 matches the desired chirp characteristic exactly. In the exponential chirp case, we varied the reference frequency according

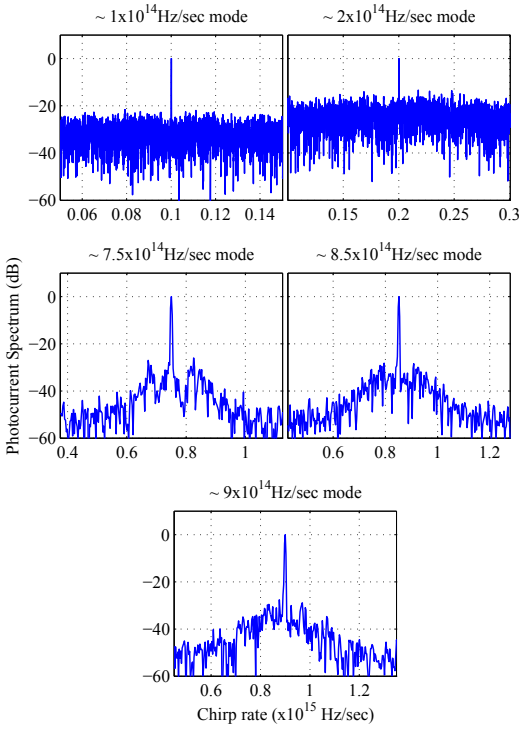

(a) 1550 nm DFB SFL

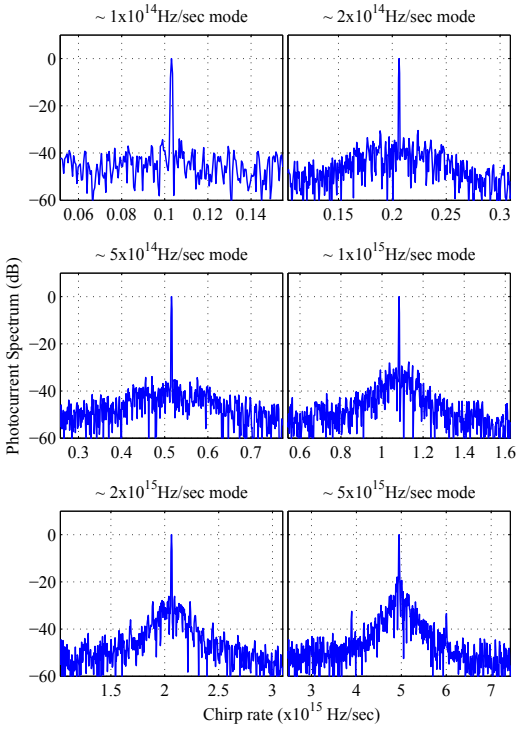

(b) 1550 nm VCSEL SFL

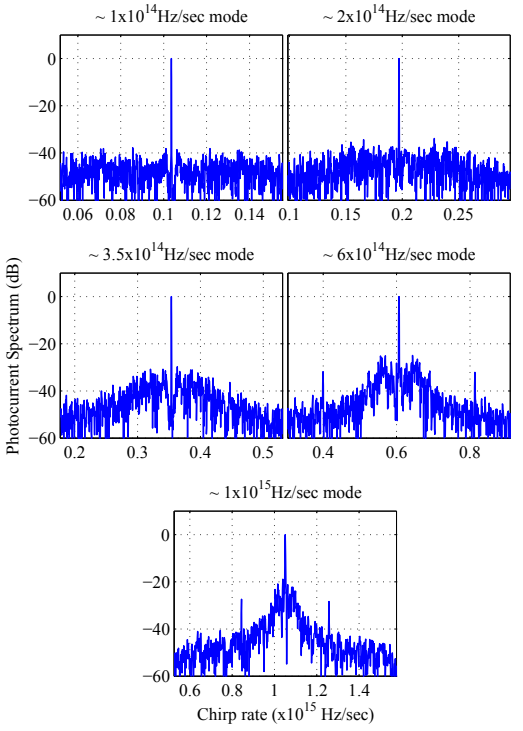

(c) 1060 nm DFB SFL

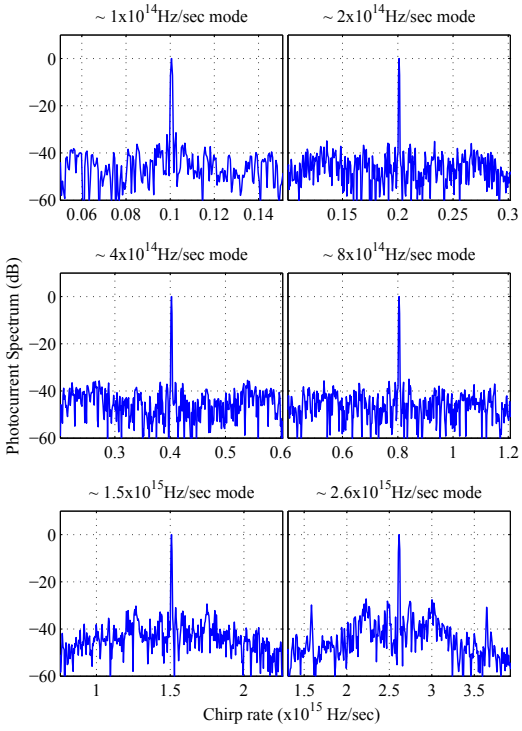

(d) 1060 nm VCSEL SFL

Figure 3.13: Locked MZI spectra of various SFLs for different values of the chirp rate ξ. The x-axis in all the plots corresponds to the chirp rate.

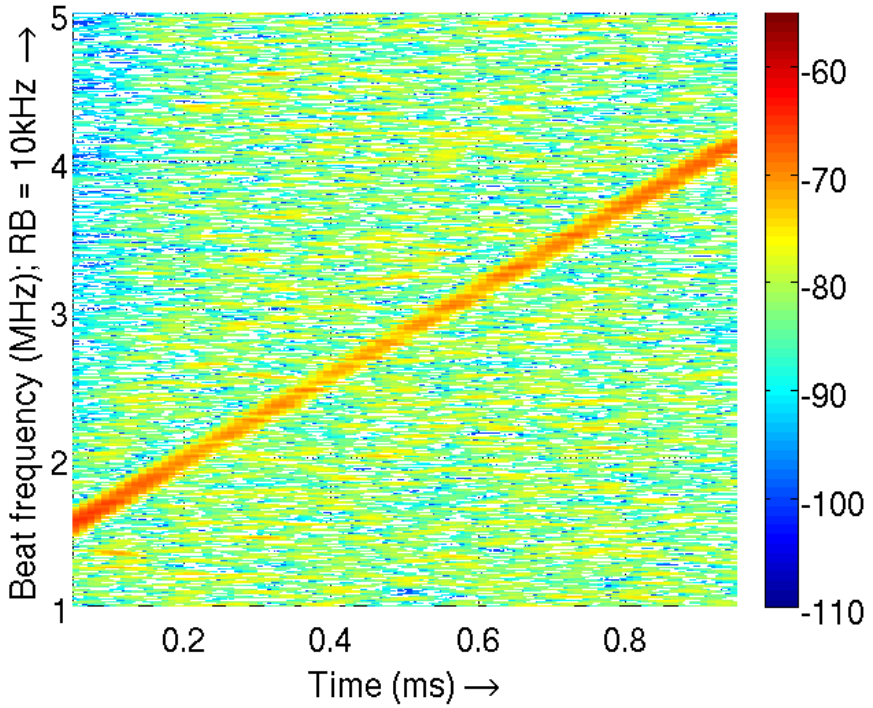

Figure 3.14: Quadratic chirp spectrogram

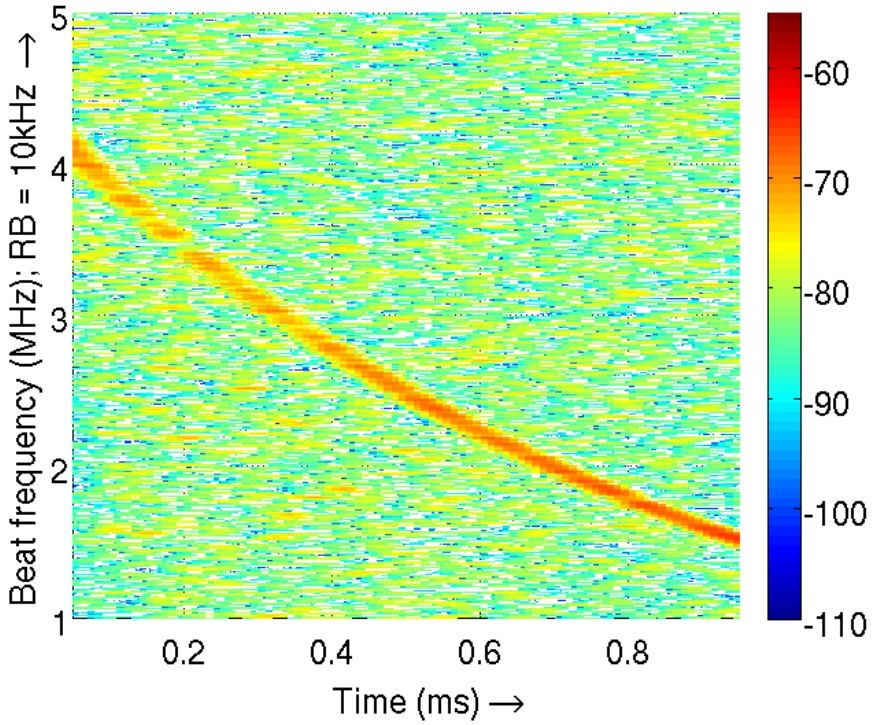

Figure 3.15: Exponential chirp spectrogram

to

$$\omega_{REF}(t) = 2\pi \times (4.29 \text{ MHz}) \times \left(\frac{1.43 \text{ MHz}}{4.29 \text{ MHz}}\right)^{t/(1 \text{ ms})}. \quad (3.20)$$

This corresponds to an exponential decrease of the optical chip rate from 150 to 50 GHz/ms. The measured photocurrent spectrogram is shown in figure 3.15. A combination of bias current predistortion and optoelectronic feedback can therefore be used for arbitrary chirp generation.

3.5 Demonstrated Applications

3.5.1 FMCW Reflectometry Using the Optoelectronic SFL

The development of the optoelectronic SFL was motivated by FMCW reflectometry and its applications in ranging and 3-D imaging (see chapter 2). The free-space depth resolution of an FMCW system is given by equation (2.8), and a bandwidth of 500 GHz corresponds to a free-space resolution of 0.3 mm. For a medium with index of refraction n, the depth resolution is given by

$$\Delta z = \frac{c}{2nB}, \quad (3.21)$$

where B is the chirp bandwidth of the SFL. We demonstrated the use of the VCSEL-based optoelectronic SFL in FMCW reflectometry by imaging acrylic sheets of varying thickness and a refractive index of 1.5 using the experimental configuration of figure 2.2. Reflections from the front and back acrylic surfaces show up as peaks in the FMCW photocurrent spectrum, shown in figure 3.16 for four sheets with nominal thicknesses of (a) 4.29 mm, (b) 2.82 mm, (c) 1.49 mm, and (d) 1.00 mm. The x-axis has been scaled to distance. The measured peak separations agree well with the nominal values. The bandwidth of the SFL was 500 GHz, corresponding to a resolution of 0.2 mm in acrylic. As a result, all of the reflection pairs shown in figure 3.16 are very well resolved.

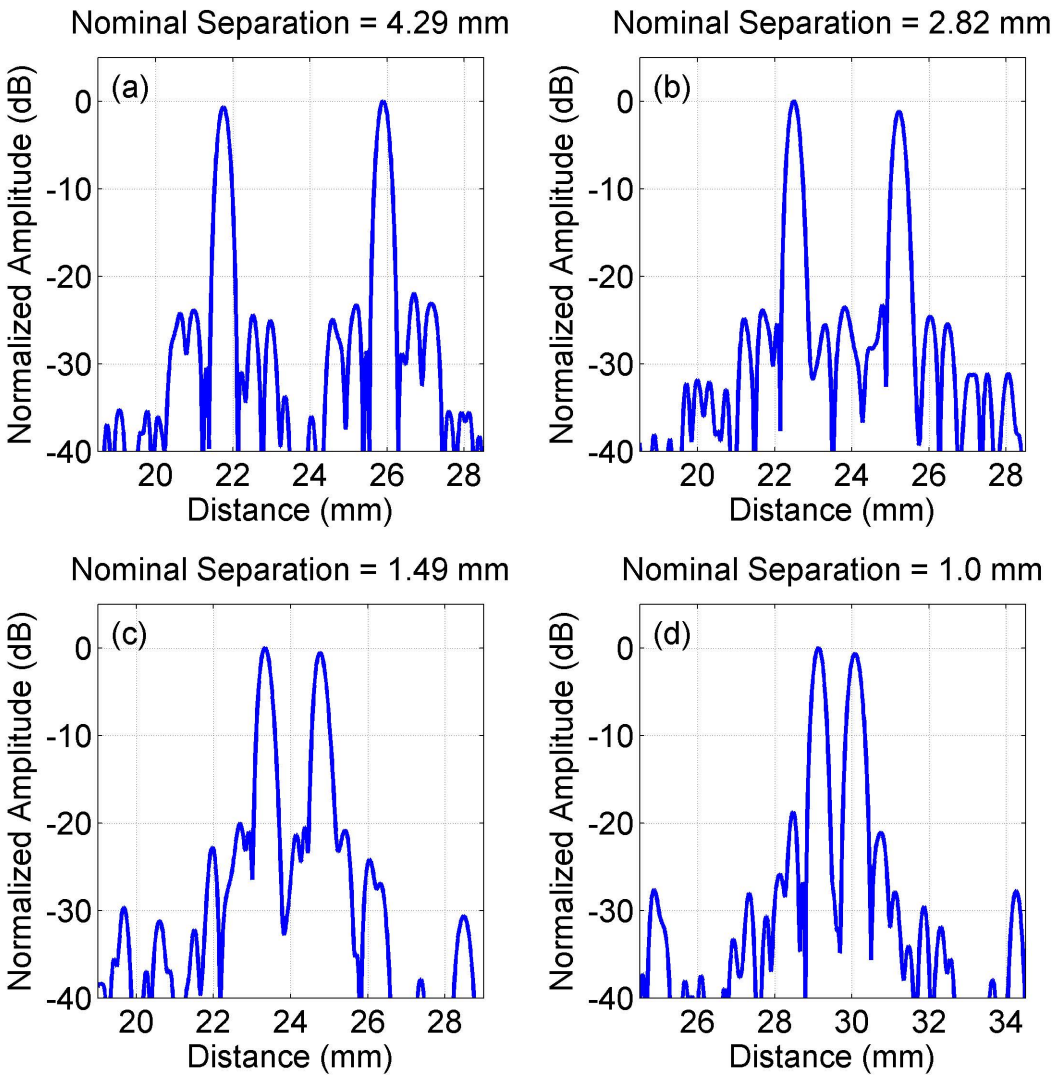

Figure 3.16: FMCW reflectometry of acrylic sheets using the VCSEL-based optoelectronic SFL with a chirp bandwidth of 500 GHz and a wavelength of ~ 1550 nm

3.5.2 Profilometry

The range resolution of an FMCW system describes its ability to tell apart reflections from closely spaced scatterers. In some imaging applications, such as profilometry, it is *a priori* known that there is only a single scatterer. The relevant metric then is not resolution, but accuracy. The accuracy of an FMCW system can be much finer than its resolution, as described in section 2.1.3.5. We demonstrate this by measuring the profile of a United States $1 coin using the VCSEL-based optoelectronic SFL with a chirp bandwidth of 500 GHz at 1550 nm. The coin was mounted on a motorized two-dimensional translation stage. The light was collimated using a gradient-index (GRIN) lens with a beam diameter of 0.5 mm. The depth at a particular transverse location was determined by measuring the strongest photocurrent frequency in a Michelson interferometer with a balanced detector (figure 2.5). The measured profile is shown in figure 3.17. As expected, we were able to record features with depth variations that are much finer than the 0.3 mm axial resolution of a 500 GHz chirp.

3.6 Summary

In this chapter we described the design of the SCL-based optoelectronic SFL. We derived equations that govern its steady-state operation, and introduced an iterative predistortion procedure that relaxes constraints on the optoelectronic feedback and enables locking at high chirp rates. We discussed different SCL platforms and how they motivate the choice of an amplitude control element. We demonstrated closed-loop linear and arbitrary chirps and established the use of the optoelectronic SFL in reflectometry and profilometry applications.

In the next chapter we examine multiple source FMCW (MS-FMCW) reflectometry, a high-resolution optical ranging technique that is enabled by the starting frequency stability and chirp control of the optoelectronic SFL.

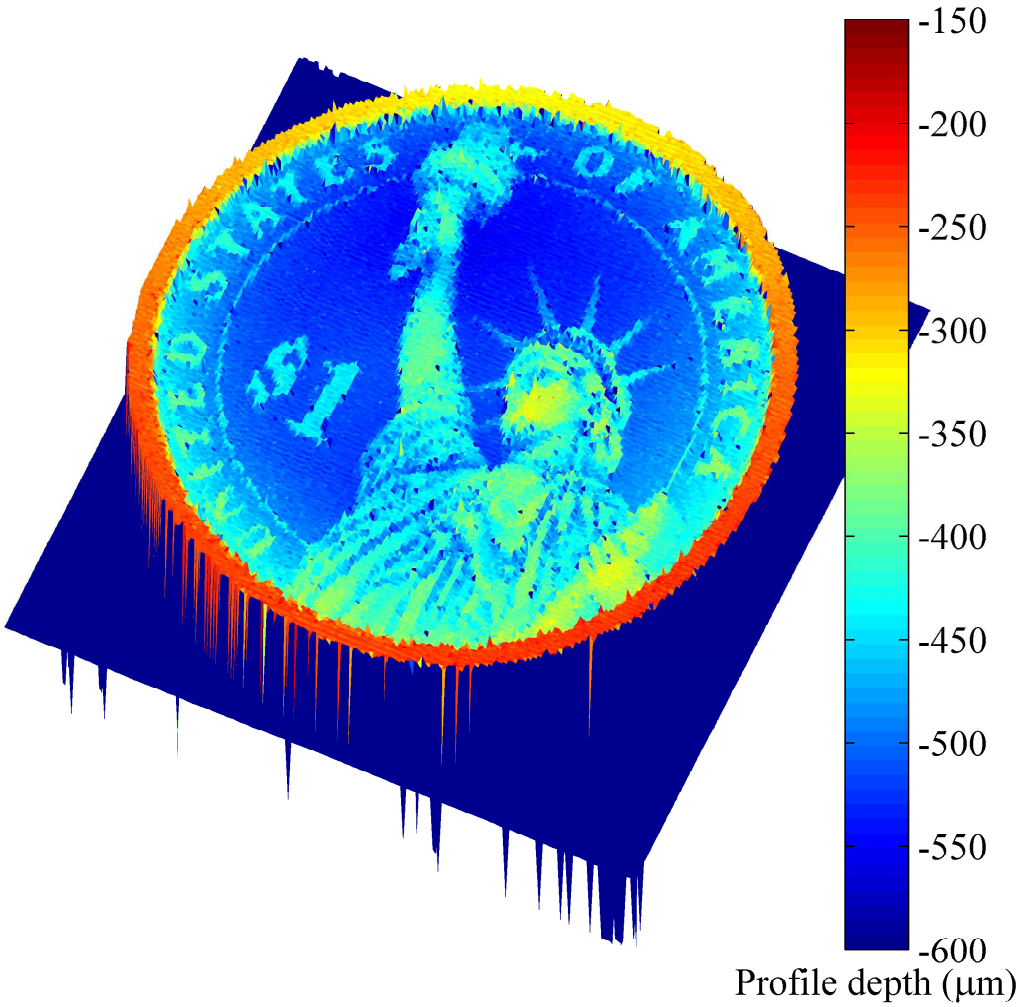

Figure 3.17: Depth profile of a United States $1 coin measured using the VCSEL-based optoelectronic SFL with a chirp bandwidth of 500 GHz and a wavelength of $\sim$ 1550 nm